J Mater Sci: Mater Electron (2023) 34:241

The structural and dynamic nanohardness properties of yttrium substituted layered (La, Ca)$_3$Mn$_2$O$_7$ manganites

N. Soylu Koc[1,*], R. Terzioglu[2], O. Ozturk[3], and C. Terzioglu[1]

[1] Department of Physics, Faculty of Arts and Sciences, Bolu Abant Izzet Baysal University, Bolu, Turkey
[2] Department of Electrical and Electronics Engineering, Faculty of Engineering, Bolu Abant Izzet Baysal University, Bolu, Turkey
[3] Department of Electrical and Electronics Engineering, Faculty of Engineering, Kastamonu University, Kastamonu, Turkey

Received: 13 June 2022
Accepted: 23 November 2022
Published online: 20 January 2023

ABSTRACT

This study devotes the structural and dynamic nanohardness properties of yttrium (Y) substituted within $La_{1.4}Ca_{1.6}Mn_2O_7$ manganites. XRD, SEM, EDS and dynamic nanohardness measurements are carried out to determine the structural properties such as grain sizes, impurity phases, crystallite sizes, average strain, and surface morphologies. The obtained results were compared with other rare-earth (RE) substituted double-layered lanthanum manganites published in the literature that have the same A-site radius. The lattice parameters are not affected substantially by the Y addition while the average grain size is significantly different from the other RE-substituted samples. The mechanical properties obtained from the dynamic micro-hardness tests such as the contact depth, area of the indent imprint, stiffness, creep, apparent hardness, reduced elastic modulus and the elastic recovery ratio (ERR) are calculated for the Y-substituted sample and compared with previously published studies. Different models are applied to determine the measured and true micro-hardness values. The microstructural and mechanical properties of Y-substituted double-layered manganites are discussed in detail.

1 Introduction

Since improvements in composite properties have been observed when the atomic size of reinforced material shrinks to the nanometer scale, researchers and industrial practitioners have become increasingly interested in nanoscience and nanotechnology [1, 2]. In the industrial sector, there is a growing need for sophisticated composite materials with improved functional qualities and performance traits. In order to define the mechanical qualities in relation to its microstructure, microhardness is a crucial metric.

Perovskite manganites have received a lot of attention lately because of their possible technological uses and unusual physical characteristics. For instance, solid oxide fuel cells, refrigerators, highly

Address correspondence to E-mail: nevinsoylu@ibu.edu.tr

https://doi.org/10.1007/s10854-022-09511-z

sensitive magnetic-field sensors, magnetic recording and readout equipment, and other technical gadgets have all been constructed with magnetic manganite materials as a crucial component. These manganites are utilized in magnetic data storage, high-sensitivity magnetic-field sensors, refrigerators, photocatalytic and thermochemical energy storage applications due to their good and unique chemical, physical, magnetic, and electrical properties [3–6].

Many types of research have been done recently on the mixed valance perovskite crystal structured manganites of $RE^{3+}{}_{x}AE^{2+}{}_{1-x}MnO_3$ [RE refers to a trivalent rare-earth element (La, Sm, Gd, etc.) and AE denotes a divalent alkaline earth element (Ca, Ba, Sr, etc.)]. Many in-depth studies have also been carried out for Ruddlesden–Popper (RP), another variation of the perovskite manganite family of the $A_{n+1}Mn_nO_{3n+1}$. The double-layer (DL) RP phase, with $n = 2$ members along the c-axis of an iterative layered as a double-layer of (MnO_2), inserted between two single layers of a non-magnetic mixture of (AO) (A alone could be La, Sr, Ca or a mixture of them). The layered perovskite manganites can be regarded as a natural "ferromagnetic metal layer–insulator layer–ferromagnetic metal layer". RP phase displays a two-dimensional Mn–O–Mn network and anisotropic magnetotransport properties [7].

Unlike simple perovskites, layered perovskite materials have high-sensitivity to very small changes in structure and composition due to their anisotropic structure by nature. For that reason, DL manganites are extremely sensitive to magnetic-field changes; internal–external pressure changes. These replaceable features of these materials allow the technology to be applied in some systems.

The mechanical properties of such manganites are important in designing and producing the applications mentioned above [8–11]. These materials should show their ability to withstand mechanical forces during production and operation procedures. Mechanical properties such as nanohardness, elastic modules, elastic recovery ratio and stiffness can be useful for this purpose and can be measured with various indentation methods like Berkovich, Vickers, etc. [12–17]. Dynamic nanohardness measurements can also be performed due to see the effects of the elastic deformation. The goal of this method is to gain information on the phase transformations, cracking and delamination as well as to determine the hardness and elastic modules [14].

The double-layered (DL) manganites have gained much more attraction since Ref. [18] discovered colossal magneto resistivity (CMR) in these materials due to anisotropic exchange interaction. The large value of low-field magnetoresistance reduced dimensionality, and structural anisotropy and the Jahn–Teller effect enabled these materials for many technological applications. The aim is to investigate and improve the structural, electronic, magnetic, electrical and mechanical properties of DL manganites. In [19] the structural and electronic properties of $LaCa_2Mn_2O_7$ manganites were analyzed and presented. It was reported that the perovskite impurity limited the magneto resistivity (MR) effect. In another study, the spin and the orbital ordering in the DL perovskite manganites were theoretically investigated [20]. Reference [21] presented the electrical and magnetic properties of DL manganites with fixed doping concentrations of rare-earth (RE) elements. The ionic radius of the A-site ($\langle r_A \rangle$) was changed by substituting the A-site with different RE ions. The electrical and magnetic properties in the DL manganites were found severely dependent on the $\langle r_A \rangle$. The A-site dependence was also found with Eu doping in [22]. The structural and magneto-electrical properties of Cu [23] and RE (La, Pr, Eu, Y and Gd) doping [24] in DL manganites were also reported in the literature. The cell parameters and volume of all samples showed an increment to increase dope content. Wang et al. investigated the magnetocaloric and electronic properties of the DL $La_{1.34}Sr_{1.66}Mn_2O_7$ manganite [25]. Reference [26] carried out sets of magnetization and magnetoresistance measurements in different temperatures, magnetic-fields and times in the Ru-doped layered manganite system. The full bulk spin polarization and intrinsic tunnel barriers at the surface of layered manganites were investigated at [27] and as a result, it was proven that they can be used as an ideal magnetic tunnel junction naturally with the creation of a surface insulator above a fully spin-polarized bulk. The preparation and low-field MR behavior of $La_{1.4}Ca_{1.6}Mn_2O_7$ was investigated and compared with an infinite layered manganite $La_{0.7}Ca_{0.3}MnO_3$ [28]. The magnetic phase diagram [29], the presence of nano-ferromagnetic domains [30] and the effect of high-temperature sintering [31] on the lanthanum manganites were also reported. Reference [32] used a model to calculate the magnetocaloric properties of DL manganites from *M*–*T* calculations under different magnetic-fields. Reddy

studied the effect of the size of lanthanide ion on bilayered $R_{1.2}Sr_{1.8}Mn_2O_7$ manganites magnetotransport properties. It was observed that the decreasing lanthanide ion size resulted in an anisotropic lattice contraction [33]. Reference [34] established a relation between local Mn charge and Mn–O distances as a function of doping and the reason for unstable structures at some doping levels of DL compounds. The cation size mismatch effect in a series of RE-substituted DL manganites was analyzed [35]. It was reported that the metal–insulator transition decreased with the decrease in the cation size and higher size variance led to lower Curie temperature.

Few studies examine the mechanical properties of DL manganites. Reference [36] reported the results of elastic constants and Debye temperature of the $R_{1.2}Sr_{1.8}Mn_2O_7$ (R = La, Pr, Nd, Sm) compound and the elastic properties were found to decrease with increasing RE ion size. A recent study [37] investigated the structural and micro-hardness properties of Gd and Nd substituted DL manganites with the same A-site radius. Both samples' lattice parameters did not change significantly, on the contrary, different average grain sizes were observed. It was reported that the hardness values increased with increasing applied load and the percentage ERR (%) of the Gd substituted sample was higher than the Nd substituted sample. The samples showed reverse indentation size effect (RISE). Finally Reference [38] presented a similar study and investigated the substitution of Pr and Sm on the A-site doping of $LaCaMnO_7$ DL manganites. The substitution affected the microstructure strongly. The hardness value of the Sm (Pr) substituted sample increased (decreased) with the load increasement and a RISE (indentation size effect ISE) was observed and the elastic recovery ratio (ERR) of the samples had opposite dependences on the load.

In this study, a Y-substituted DL manganite $(La_{0.67}Y_{0.33})_{1.4}Ca_{1.6}Mn_2O_7$ with a Y-substituted DL manganite with a similar A-site radius to [37] and [38] is synthesized in this study in order to demonstrate and compare the structural and mechanical properties. Nd, Gd, Pr, and Sm are all RE elements, but Y is not a lanthanide like the others, which is why it was chosen for substitution and contrasted with those elements. Y (transition metal) is a chemical element that is composed of atoms having unpaired d electrons, while lanthanides have valence electrons in their 4f orbital. XRD, SEM data and the dynamic indentation measurements of the sample is carried out. To the best of our knowledge, there is no detailed study that examines the effect of Y substitution with A-site and comparison with other RE substitution on the structural and mechanical properties of DL lanthanum manganites in the literature.

2 Experimental procedures

A bulk DL manganite with Y substitution to La site in the form of $(La_{1-y}Y_y)_{1.4}Ca_{1.6}Mn_2O_7$ and with an average A-site radius of approximately 1.32 Å is produced similarly as in [37] and [38]. The A-site radius was achieved by the calculation according to Shannon's ionic radii table with a 12-coordination number [39]. According to this calculation, our chemical formulation is $(La_{0.67}Y_{0.33})_{1.4}Ca_{1.6}Mn_2O_7$. (The ionic radius of Y^{3+} is 1.18 Å, the density value for the Y element is 4.47 g/cm^3 while the lattice parameters a and c are a = 3.65 Å, c = 5.73 Å [22].) The Y-substituted DL manganite is named LYCMO. The Gd, Nd, Pr and Sm substituted samples presented in the literature before, will be named LGCMO [37], LNCMO [37], LPCMO [38] and LSCMO [38], respectively for comparison. The solid-state reaction process was used in the preparation of the sample. The calculated quantities of Y_2O_3, $CaCO_3$ and MnO_2 (all 99.99%) were mixed and preheated. Then the powder was ground and calcined at 900 and 1000 °C for 12 and 20 h, respectively. The mixture was re-grinded and turned into a pellet under 2.7216 metric tons. Then the pellet was sintered twice (1150 °C for 24 h and 1250 °C for 24 h). Finally, an annealing process was done with a small cooldown rate to room temperature (RT) at 800 °C for 10 h.

XRD data were collected to obtain the crystallographic structure of the sample at RT with the usage of a Rigaku diffractometer with Cu Kα radiation (λ = 1.5418 Å). The diffraction angle values were between 20° and 80° with a speed of 3 per minute. The sensitivity of the scan was 0.02°. The Le Bail refinement was used in calculating the impurity phase structure using the Jana 2006 software [40] and also the crystallite size, lattice parameters were obtained through the recorded XRD data utilizing Debye–Scherrer's formula as [41], $D = (K\lambda/\beta\cos\theta)$ where D is the size of the crystal, K is known as the Scherrer's constant (K = 0.94), depends on the crystallite shape and the size distribution. λ is the X-ray

wavelength (1.54178 Å), β is full width at half maximum (FWHM) of the diffraction peak or integral breadth [42] and θ is the angle of diffraction [43]. K can have values anywhere from 0.62 to 2.08. In this paper, $K = 0.94$ was used. The microstrain in the crystallite or nanocrystal also affects the width β, which needs to be considered in an accurate analysis. Spatial fluctuations in the alloy composition can also affect the width. In this work, the calculated values of D represent estimates. The average strain (ε), numerical expression of broadening in XRD peaks due to crystal imperfections or distortions, was also calculated by exploiting the Williamson–Hall equation (W–H), $\varepsilon = \beta/4\tan\theta$ [44, 45].

The particle size and surface morphology of the Y-substituted DL manganite were determined with the usage of the JSM 6390 LV-JEOL model (SEM) at an acceleration voltage of 20 kV. Average particle sizes were calculated by pattern analysis. The semi-quantitative analysis of the sample was obtained with an Oxford Model 550i energy dispersive X-ray (EDX) spectroscopy.

A UMT-Bruker SYS2 mechanical tester was used for the determination of mechanical parameters. A Vickers-type indenter was used and the measurements were done at different applied forces between 0 and 2000 mN for 10 s at room temperature [16]. A force is applied to the samples and simultaneously the trace left in the sample is measured. At the maximum load value, the load is kept constant to see the sample behavior. The contact depth–load curves were obtained from these measurements. Mechanical parameters were determined from these measurement results and explained in Sect. 3.2 in detail.

3 Results and discussion

3.1 XRD, SEM and EDX results

XRD data and the parameters such as lattice parameters, the goodness of fit (GOF) and crystallite size, and average strain of the $(La_{0.67}Y_{0.33})_{1.4}Ca_{1.6}Mn_2O_7$ sample are presented in Fig. 1 and Table 1, respectively. The refinement result has been obtained using crystallizes in the tetragonal structure with the I4/mmm space group parameters similar to other same A-site RE-substituted DL manganite in [37] and [38]. The patterns of reflections at 27°, 33°, 43° and 23.6° were observed and are unique to the $n = 2$ phase

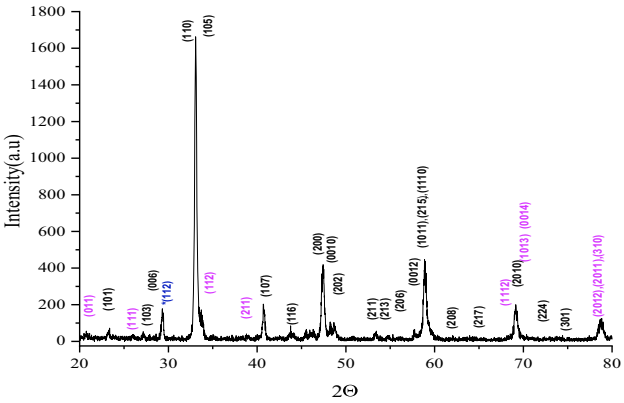

Fig. 1 XRD patterns of the LYCMO sample

Table 1 The structural parameters of LYCMO

Tetragonal structure	
Space group *I4/mmm*	
$\langle r_A \rangle$=1.32 Å	
	LYCMO
a (Å)	3.831
c (Å)	18.972
V (Å^3)	278.5
GOF	0.87
R_p	12.62
R_{wp}	18.47
$\langle D \rangle$ (nm)	24
ε	2.77×10^{-3}

[46, 47]. Small quantities of secondary additional phase ((La, Ca)MnO_3) (space group *Pnma*) were found in the LYCMO sample (the purple-coloured indices). The superposition of the experimental and the calculated pattern of LYCMO is shown in Fig. 2. And also, there is a peak (112) of the Mn_3O_4 impurity phase at $2\Theta = 29.25°$ [48]. The calculated cell parameters are similar to the parameters reported by many other studies for DL lanthanum manganites [24, 28, 30, 31, 49]. From the values given in Table 2, it can be seen that there is no significant difference between the volumes of the unit cells of the Y- and Gd, Nd, Pr, and Sm substituted samples. Finding similar unit cell volume is due to the constant A-site ionic radius. The GOF value of the LYCMO sample is 0.87 and smaller compared to all other RE-substituted DL manganites with the same $\langle r_A \rangle$ which indicates that LYCMO has fewer impurities. The LYCMO sample has a smaller crystallite size, (Tables 1, 2) compared to the LGCMO/LNCMO/LPCMO/

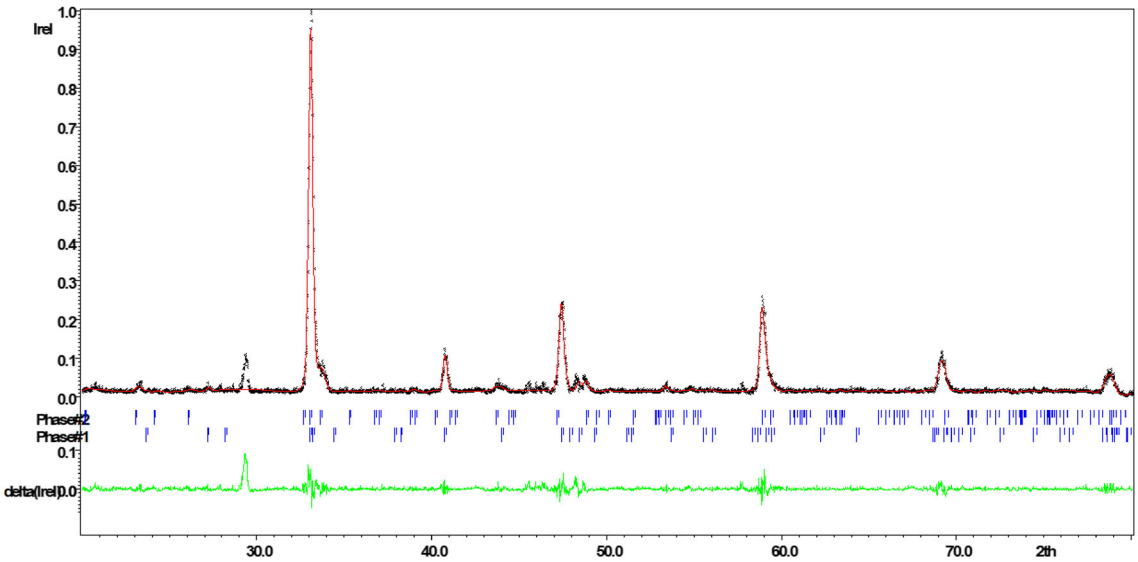

Fig. 2 The Le Bail refinement and experimental data fitting of the LYCMO sample. The lines just below the patterns correspond to the difference. The bottom vertical bars are Bragg positions for $(La_{0.67}Y_{0.33})_{1.4}Ca_{1.6}Mn_2O_7$, the top is for (La, Ca)MnO_3 and the secondary phase

Table 2 The comparison of structural parameters

Sample	Structure	Unit cells		GOF	Crystallite size (nm) $\langle D \rangle$	Grain size (μm)
		a (Å)	c (Å)			
LYCMO	Tetragonal	3.831	18.972	0.87	24	1.71
LGCMO [37]	Tetragonal	3.844	19.220	1.05	40	1.40
LNCMO [37]	Tetragonal	3.849	19.305	1.96	37	0.84
LPCMO [38]	Tetragonal	3.870	19.388	1.44	61	1.61
LSCMO [38]	Tetragonal	3.858	19.295	1.14	53	1.43

LSCMO samples. Also, the crystallite size of LYCMO (24 nm) has a smaller crystallite size than the LCMO (≥ 35 nm) manganite [50] and the $La_{1.4}Ca_{1.6}Mn_2O_7$ DL manganite [31].

The crystallite size and the grain size values are completely different parameters in which the grain size is bigger than the crystallite size [51]. Also, the calculations of these parameters are different. The crystallite size is obtained using the XRD data while the grain size is found from SEM images. The average particle size of the DL LYCMO sample is calculated by the usage of the ImageJ software and based on the Gaussian fitting method the average particle size is calculated to be 1.71 μm. From the micrographs, uniform granularity was observed, grains were bright and visible, and the particle boundaries are irregular but almost clear. The average grain size for the LYCMO sample obtained from Fig. 3 is about 3.10 μm. The LYCMO sample has a larger average grain size than the LGCMO/LNCMO/LPCMO/LSCMO samples reported in [37] and [38]. Moreover, the number and the size of voids at the surface of the LYCMO sample are more in comparison with LGCMO/LNCMO/LPCMO/LSCMO samples.

It is noteworthy to say that substitution with rare-earth elements of similar ionic radii affects the microstructure in different ways. Based on the structural results, it is expected that the larger grain size and lower impurities would make the hardness value lower compared to other RE-substituted DL manganites reported in the literature.

The results obtained from the EDX measurements show that all the elements used in the preparation process are detected as shown in Fig. 3. Also, the weight percentages of the elements in LYCMO are listed in Table 3.

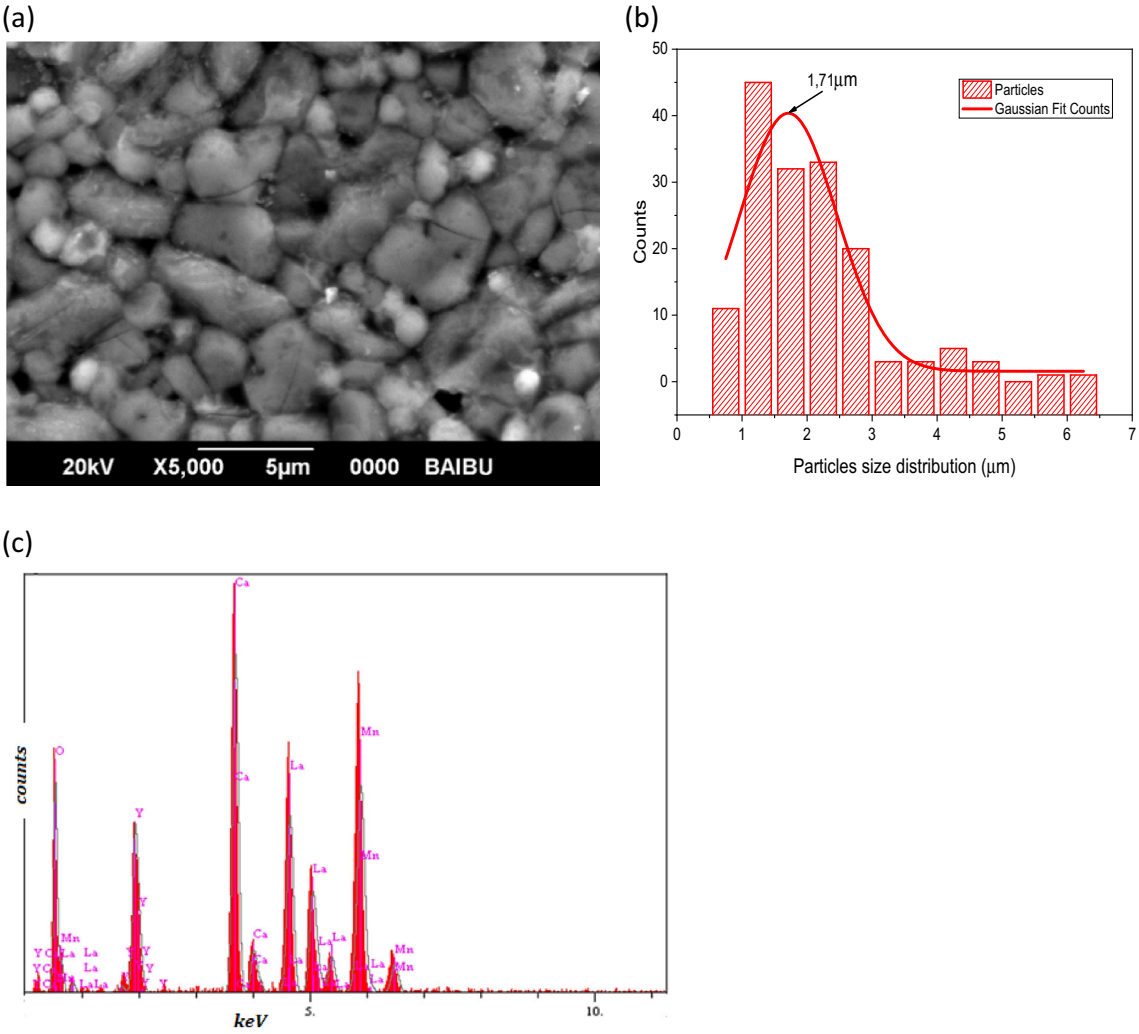

Fig. 3 **a** SEM image, **b** particle size distribution image, and **c** EDX map of LYCMO

Table 3 The elemental composition (wt%) of LYCMO

Concentration (%) LYCMO	
Element	%
O	27.443
Ca	11.521
Mn	13.756
La	14.558
Y	32.722
	100.000

3.2 Hardness measurements

The conventional hardness tests cannot examine the elastic deformation effects while Vickers micro-indentation tests enable the determination of elastic modulus (E) and micro-hardness (H) by considering plastic and elastic deformations. The loading/unloading–penetration depth curves determined from the dynamic indentation tests are used and the sample is exposed to elastic and plastic deformation during these measurements. The final contact depth (h_f) and the maximum contact depth (h_{max}) are determined after the load removal and during the load, respectively. Before the calculation of E and H, the maximum load applied to the sample (P_{max}), the indent imprint area (A_c) and the stiffness (S) must be determined. Hereafter P is the applied load, h is the indentation diagonal length and h_f is the final depth.

The penetration depth–load/unload dependency for LYCMO at different applied loads is presented in Fig. 4. The scatters seen in the figure may have been caused by the nonuniform structural properties of LYCMO.

The indent imprint (A_c) is calculated with $A_c = \pi hc^2 \tan^2 \alpha$ where $\alpha = 70.3°$ for a Vickers and Berkovich indenter and h_c is the contact depth calculated from fitting the initial part of the unloading curve. For the Vickers micro-indentation test, the area can be calculated as,

$$A_c = 24.5 {h_c}^2. \quad (1)$$

The method found in [12] is used to determine the contact depth by fitting the unloading curve to an empirical power-law relation ($P = \alpha(h - h_f)^m$). The derivation of this relation is used to calculate the stiffness [13],

$$S = \left|\frac{dP}{dh}\right| = \frac{2}{\sqrt{\pi}} E_r \sqrt{A_c}, \quad (2)$$

where E_r is the reduced elastic modules.

The indentation contact depth (h_c) and the contact area (A_c) of the sample under different loads were calculated and are displayed in Table 4. Similar to [37] and [38], h_c and A_c values of LYCMO increase with increasing applied load. The variation of LYCMO's h_c is similar to LNCMO and lower than LGCMO, LPCMO and LSCMO. This provides information that LYCMO will have more elastic recovery than the other samples. Intercalary, the values of h_{max} of LYCMO were found to be 17.90 and 22.21 µm at 400 mN and 2000 mN. Compared to LGCMO, LNCMO, LPCMO and LSCMO, the h_{max} of LYCMO at 2.0 N is only lower than that of LPCMO while the h_{max} at 0.4 N is higher than all other samples.

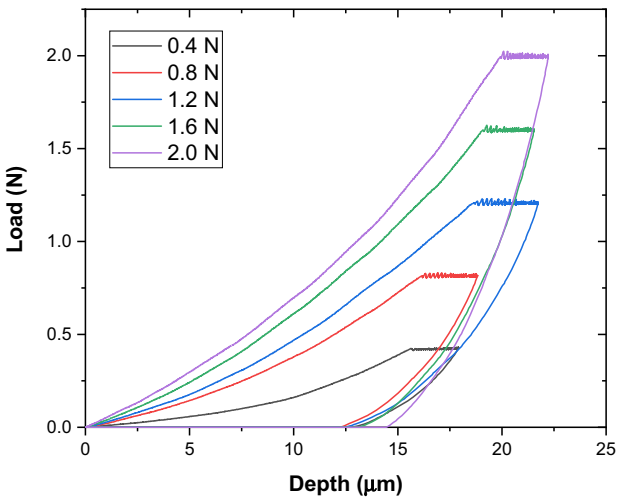

Fig. 4 The loading/unloading–depth curve of the substituted LYCMO

Stiffness (S) is the rigidity of structural material. The stiffness values calculated using Eq. 2 for LYCMO are shown in Table 4. The values of S for LYCMO are load-dependent and have a directly proportional behavior with the applied load. Moreover, the S value of LYCMO is in the same range as LSCMO at 2000 mN and smaller than those of L(G, N, P)CMO. This result also indicates that the ERR of LYCMO and LSCMO is higher than that of LGCMO, LNCMO and LPCMO at 2000 mN.

Creep is the propensity of a material to pursue deforming under a constant force and is an important mechanical property [50]. In our study, the applied load was kept constant for 10 s when it was at its maximum value. In all load values, the creep behavior was observed despite the constant applied load, the indenter continued increasing the indented area. The creep values are presented in Table 4. The creep values of LYCMO do not have a systematical behavior. The creep behavior might be caused by the material type because other parameters such as applied load, time that the load was kept constant, and loading rate and temperature [16, 17] are the same.

Pop-in (pop-out) is a notion that is sometimes observed at nanoindentation tests where an abrupt displacement appears in the loading (unloading) curve and can be affected by many parameters such as grain boundaries, surface roughness, etc. [52]. LYCMO did not show any pop-in or pop-out behavior.

The micro-indentation hardness is calculated by [12],

$$H = \frac{P_{max}}{A_c} = \frac{P_{max}}{24.5 {h_c}^2}. \quad (3)$$

The calculated micro-hardness and reduced elastic modulus values are presented in Table 4. The load dependency of these values for LYCMO and comparison to other RE-substituted manganites are presented in Figs. 5 and 6, respectively. The results indicate that both parameters are load-dependent. The H and E_r values for the LYCMO increased with increasing applied load. Moreover, the values of $H(E_r)$ for the LYCMO sample are 0.064 GPa (2.345 GPa), 0.121 GPa (3.678 GPa), 0.14 GPa (3.783 GPa), 0.19 GPa (5.148 GPa) and 0.219 GPa (6.385 GPa) at 0.4 N, 0.8 N, 1.2 N, 1.6 and 2.0 N, respectively. The LYCMO has the lowest hardness values at low

Table 4 h_c, A_c, creep, S, H and E_r values for LYCMO

P_{max} (N)	h_c (μm)	h_{max} (μm)	A_c (m^2)	Creep (μm)	S (N/μm)	H (GPa)	E_r (GPa)
0.4	15.99	17.90	6.265×10^{-9}	2.03	0.210	0.064	2.345
0.8	16.00	18.20	6.633×10^{-9}	2.55	0.338	0.121	3.678
1.2	18.70	21.74	8.571×10^{-9}	2.95	0.395	0.140	3.783
1.6	18.53	21.53	8.409×10^{-9}	2.28	0.533	0.190	5.148
2.0	19.31	22.21	9.136×10^{-9}	2.25	0.689	0.219	6.385

applied loads. This can be because Y has a lower density, cell parameters and ionic radius than Gd, Nd, Pr and Sm [47, 53].

Figure 5, indicates that the apparent hardness increased with the increase in applied loads for all samples named the reverse indentation size effect (RISE) [54, 55], excluding LPCMO. RISE behavior has been explained by multiple factors in previous studies [55–58]. The LPCMO's hardness dependency showed contrary behavior [38] called the indentation size effect (ISE).

The experimental data of apparent hardness is used to obtain the true hardness values for the sample. In the literature, it is well known that the best model for calculating the true hardness of samples that shows the RISE behavior is the indentation-induced cracking (IIC) model [58]. The Hays Kendall model was used in [38] for the LPCMO sample because it showed ISE behavior. To obtain the true hardness with the IIC model the experimental data are fitted by Eq. 4:

$$H_{IIC} = K(P^{5/3}/h_c{}^3)^m, \quad (4)$$

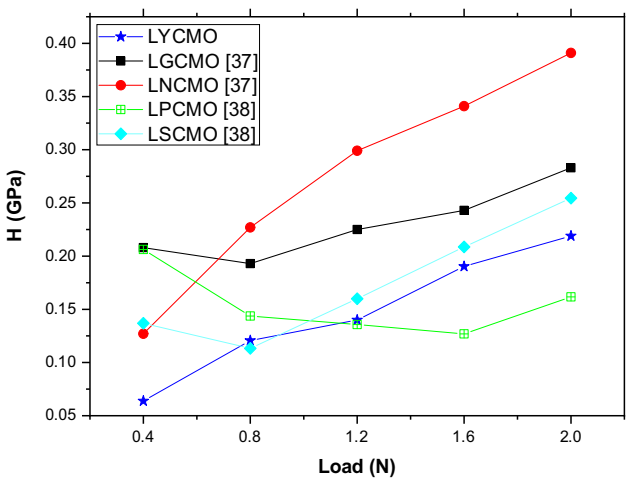

Fig. 5 Hardness–applied load curves of LYCMO and reported in [37, 38]

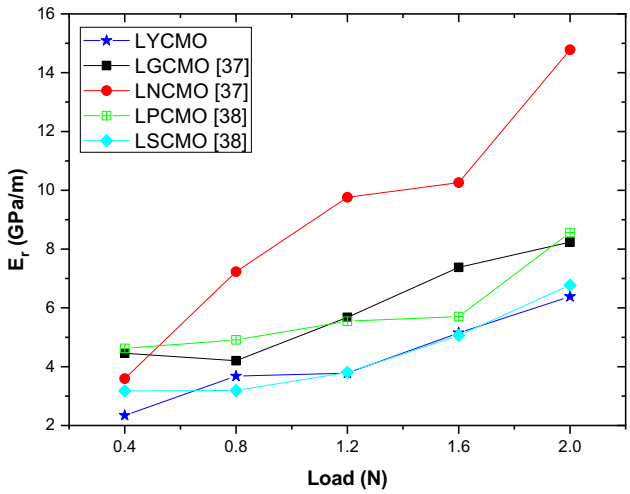

Fig. 6 Elastic modulus–applied load curves of LYCMO and reported in [37, 38]

where m is a parameter that gives information about the hardness behavior and is calculated from the slope of the $\ln(H)$–$\ln(P^{5/3}/h_c{}^3)$ curve. The true hardness (H_{IIC}) values are calculated from the same graph vertical intercept. The m value of the model is evaluated in Fig. 7. The m parameter for LYCMO is 0.582 ($m < 0.6$) which confirms that the sample show RISE behavior [59], and is in agreement with the results found in Fig. 5. The calculated H_{IIC} hardness value is 2.978 GPa for the LYCMO sample. It is obvious from the H_{IIC} value and Fig. 5 that the load values applied in this study are not enough to reach the plateau region.

To examine and compare the elastic behavior of the LYCMO sample with the samples in [37] and [38], a quantitative parameter (ERR) was used. The ERR can be calculated as [60],

$$\mathrm{ERR} = \frac{h_{max} - h_{min}}{h_{max}}.100, \quad (5)$$

where h_{max} is the maximum and h_{min} is the final depth value during the indentation tests.

Figure 8 presents the calculated ERR's for LYCMO and other RE-substituted DL samples. The calculated

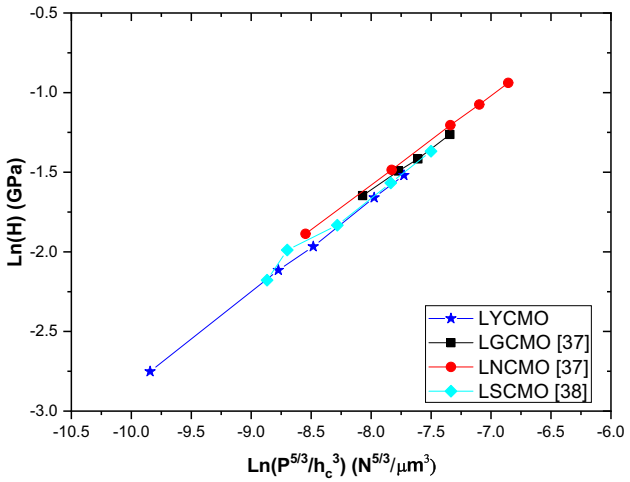

Fig. 7 $\ln(H)$–$\ln(P^{5/3}/h_c^3)$ curve

ERR value for LYCMO is in the range of 50–67%. Compared to other RE-substituted samples, LYCMO recovers better at all applied loads. The response each sample gives to occurring plastic deformation is different in all samples despite having the same A-site radii due to structural differences and particle sizes.

It is well seen that samples with the same A-site radius have roughly similar chemical and physical structures while their hardness and ERR values show quite differences. The reason for this might be deduced from the SEM measurements of the samples and the atomic properties of the substituted RE elements. These observations might all contribute to the difference in hardness in reaction to the applied load.

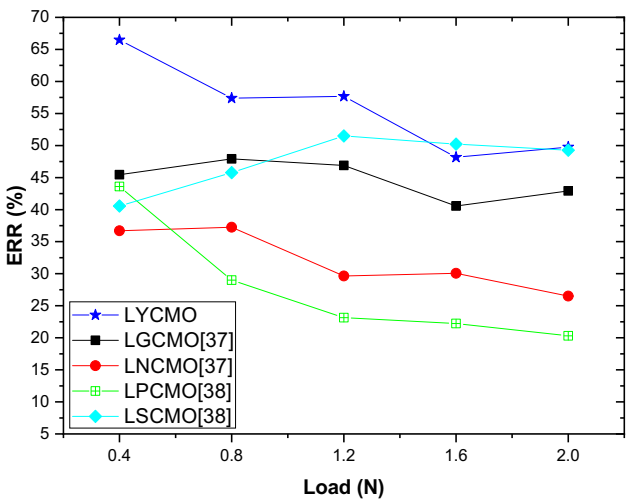

Fig. 8 ERR for the LYCMO and other samples reported in the literature at different loads

4 Conclusion

The application of strong magnetic-fields during magnetoresistance (MR) measurements have been shown to place large stresses on solid magnetoresistance materials. Recent studies are very important for the determination of the elastic modulus of polycrystalline materials, bonding forces and thermodynamic properties of solid materials [61, 62]. It is also important to investigate the elastic properties of manganite materials, where mostly magnetic and electrical properties are investigated, in order to find the appropriate material in polycrystalline material applications in technology. This study is important in terms of microhardness properties, which are rarely investigated in manganite materials.

In this study, the effect of Y substitution on the microstructural and mechanical properties of DL manganites was examined and compared with other RE substitutions published in the literature with a fixed $\langle r_A \rangle$. The microstructural investigations consisted of XRD, EDX and SEM while the mechanical investigations were done with the dynamic Vickers hardness measurements and modeling. The main findings of the study can be summarized as follows:

- The results obtained from the XRD and EDX measurements showed that the LYCMO sample crystallizes in the tetragonal structure similar to the RE-substituted DL manganites with the same $\langle r_A \rangle$ published in [37] and [38], and all the elements used in the preparation process are detected. In this respect, the crystallite size is 24 nm, the grain size is 1.71 μm, the strain value is 2.78×10^{-3}, the cell parameters are a (3.831 Å) and c (18.972 Å) and the GOF parameter value is 0.87 of LYCMO sample, and all these values are compatible with other shared values in the literature before.
- The microhardness values of the LYCMO sample increased with increasing applied load and we have found that the H_{IIC} value is 2.978 GPa which indicates that the maximum test load of 2 N used in this experiment is not enough for reaching the plateau region of the sample.
- The h_c (from 15.99 to 19.3 μm), A_c (from 6.265×10^9 to $9.136\ 10^9$ m^2), E_r (from 2.345 to 6.385 GPa) and S (from 0.21 to 0.689 N/μm) values of LYCMO increased with the increasing applied load.

- The ERR (in the range of 50–67%) of LYCMO was determined higher than 50% at all applied loads. In Fig. 8 comparison with solids of the same properties in terms of their ability to recover to their original shape) we can deduce that LYCMO has a high ability about the return to its initial shape.
- The LYCMO sample's microhardness values grow as more stress was applied, the true hardness (H_{IIC}) value is 2.978 GPa.
- In previous studies, which we also compared in detail here, since the sample LYCMO has a similar chemical and physical structure as compared with [37, 38]. One could ask for the correlation between the structural properties and hardness values. A possible answer to this question might be deduced from the SEM and density measurements. As mentioned in Sect. 3, SEM micrographs of the LYCMO sample display a less dense surface, larger grain size, higher void density, better grain connectivity and lower impurities compared to the samples in [37, 38]. These observations might all contribute to the difference in hardness in reaction to the applied load.

Author contributions

All authors contributed to the study's conception and design. Material preparation, data collection and analysis were performed by NSK and ÖÖ. The first draft of the manuscript was written by NSK and RT, and all authors commented on previous versions of the manuscript. All authors read and approved the final manuscript.

Funding

The authors have not disclosed any funding.

Data availability

The datasets generated during and/or analyzed during the current study are available from the corresponding author on reasonable request.

Declarations

Conflict of interest The authors declare that they have no known competing financial interests or personal relationships that could have appeared to influence the work reported in this paper.

References

1. Z. Raddaoui, S. El Kossi, B. Smiri, T. Al-Shahrani, J. Dhahri, H. Belmabrouk, Raman scattering and red emission of Mn^{4+} in $La_{0.7}Sr_{0.25}Na_{0.05}Mn_{0.7}Ti_{0.3}O_3$ manganite phosphor for LED applications. RSC Adv. **10**(40), 23615–23623 (2020). https://doi.org/10.1039/D0RA04033A
2. R. Brahem, Z. Raddaoui, M. Bourguiba, Effect of A-site rare earth substitution on structural, colossal permittivity, and impedance properties of $La_{0.67}R_{0.03}Ca_{0.2}Sr_{0.1}MnO_3$ (R = Pr, Er) manganite. J. Mater. Sci. Mater. Electron. **33**(7), 4156–4169 (2022). https://doi.org/10.1007/s10854-021-07611-w
3. B.F. Yu, Q. Gao, B. Zhang, X.Z. Meng, Z. Chen, Review on research of room temperature magnetic refrigeration. Int. J. Refrig. **26**(6), 622–636 (2003). https://doi.org/10.1016/S0140-7007(03)00048-3
4. M.A.-A. Mamun, A. Haque, A. Pelton, B. Paul, K. Ghosh, Structural, electronic, and magnetic analysis and device characterization of ferroelectric–ferromagnetic heterostructure (BZT–BCT/LSMO/LAO) devices for multiferroic applications. IEEE Trans. Magn. **54**(12), 2502908 (2018)
5. M. John Abel, A. Pramothkumar, V. Archana, N. Senthilkumar, K. Jothivenkatachalam, J. Joseph Prince, Facile synthesis of solar light active spinel nickel manganite ($NiMn_2O_4$) by co-precipitation route for photocatalytic application. Res. Chem. Intermed. **46**(7), 3509–3525 (2020). https://doi.org/10.1007/s11164-020-04159-y
6. D. Yilmaz, E. Darwish, H. Leion, Utilization of promising calcium manganite oxygen carriers for potential thermochemical energy storage application. Ind. Eng. Chem. Res. (2021). https://doi.org/10.1021/acs.iecr.0c05182
7. K. Raju, M.S. Song, J.Y. Lee, Crystal structure and magnetic properties of $La_{2-x}(Sr_{0.5}Ca_{0.5})_{1+x}Mn_2O_7$ (x = 0.6, 0.8 and 1.0) Ruddlesden–Popper manganites. J. Magn. Magn. Mater. **358–359**, 119–122 (2014). https://doi.org/10.1016/j.jmmm.2014.01.040
8. C. Thiele, K. Dörr, O. Bilani, J. Rödel, L. Schultz, Influence of strain on the magnetization and magnetoelectric effect in $La_{0.7}A_{0.3}MnO_3$ PMN-PT (001) (A = Sr, Ca). Phys. Rev. B **75**(5), 054408 (2007).https://doi.org/10.1103/PhysRevB.75.054408
9. Y.S. Reddy, P. Kistaiah, C. Vishnuvardhan Reddy, Elastic properties of double layered manganites $R_{1.2}Sr_{1.8}Mn_2O_7$ (R =

La, Pr, Nd, Sm). Rare Met. **33**(2), 166–170 (2014). https://doi.org/10.1007/s12598-013-0128-8

10. Y.S. Reddy, V.P. Kumar, E. Nagabhushanam, P. Kistaiah, C.V. Reddy, Electrical, magnetic and elastic properties of $La_{1.2}(Sr_{1-x}Ca_x)_{1.8}Mn_2O_7$ ($0.0 \leq x \leq 0.4$). J. Alloys Compd. **440**(1–2), 6–12 (2007). https://doi.org/10.1016/j.jallcom.2006.08.325
11. J.J.U. Buch et al., Structural and elastic properties of Ca-substituted $LaMnO_3$ at 300 K. J. Phys. D **41**(2), 025406 (2-008). https://doi.org/10.1088/0022-3727/41/2/025406
12. W.C. Oliver, G.M. Pharr, An improved technique for determining hardness and elastic modulus using load and displacement sensing indentation experiments. J. Mater. Res. **7**(6), 1564–1583 (1992). https://doi.org/10.1557/jmr.1992.1564
13. K. Zeng, C.H. Chiu, An analysis of load–penetration curves from instrumented indentation. Acta Mater. **49**(17), 3539–3551 (2001). https://doi.org/10.1016/S1359-6454(01)00245-2
14. A.C. Fischer-Cripps, Chapter 2. In *Nanoindentation* (Springer, New York, 2002)
15. A. Fischer-Cripps, D. Nicholson, Nanoindentation. Mechanical engineering series. Appl. Mech. Rev. **57**(2), B12 (2004)
16. S. Kaya, D. Akcan, O. Ozturk, L. Arda, Enhanced mechanical properties of yttrium doped ZnO nanoparticles as determined by instrumented indentation technique. Ceram. Int. **44**(9), 10306–10314 (2018). https://doi.org/10.1016/j.ceramint.2018.03.038
17. M.R. Vanlandingham, N.K. Chang, P.L. Drzal, C.C. White, S.H. Chang, Viscoelastic characterization of polymers using instrumented indentation. I. Quasi-static testing. J. Polym. Sci. B **43**(14), 1794–1811 (2005). https://doi.org/10.1002/polb.20454
18. Y. Moritomo, A. Asamitsu, H. Kuwahara, Y. Tokura, Giant magnetoresistance of manganese oxides with a layered perovskite structure. Nature **380**, 141–144 (1996). https://doi.org/10.1038/380141a0
19. M.A. Green, D.A. Neumann, Synthesis, structure, and electronic properties $LaCa_2Mn_2O_7$. Chem. Mater. **12**(1), 90–97 (2000). https://doi.org/10.1021/cm991094i
20. R. Maezono, N. Nagaosa, Spin and orbital ordering in double-layered manganites. Phys. Rev. B **61**(3), 1825–1830 (2000). https://doi.org/10.1103/PhysRevB.61.1825
21. J. Dho, W.S. Kim, H.S. Choi, E.O. Chi, N.H. Hur, Chemical pressure effects of cation size variation in layered manganites. J. Phys. Soc. Jpn **70**(8), 2448–2453 (2001). https://doi.org/10.1143/JPSJ.70.2448
22. R. Xing, W.Q. Wang, Y. Lu, J.J. Zhao, Field-induced first-order ferromagnetic transition in $(La_{0.8}Eu_{0.2})_{4/3}Sr_{5/3}Mn_2O_7$ single crystal. Main Group Chem. **18**(1), 55–62 (2019). https://doi.org/10.3233/MGC-180265
23. N. Mahamdioua et al., Structural and magneto-transport properties of copper doped double layered manganites $La_{1.4}Ca_{1.6}Mn_2O_7$. J. Supercond. Nov. Magn. **26**(5), 1441–1444 (2013). https://doi.org/10.1007/s10948-012-2024-0
24. N. Mahamdioua, A. Amira, S.P. Altintas, A. Varilci, C. Terzioglu, Effect of re doping on structure and magneto-electrical properties of $La_{1.2}Re_{0.2}Ca_{1.6}Mn_2O_7$ manganites. Physica B **429**, 12–17 (2013). https://doi.org/10.1016/j.physb.2013.07.027
25. A. Wang, Y. Liu, Z. Zhang, Y. Long, G. Cao, Magnetic entropy change and colossal magnetoresistance effect in the layered perovskite $La_{1.34}Sr_{1.66}Mn_2O_7$. Solid State Commun. **130**, 3–4 (2004). https://doi.org/10.1016/j.ssc.2003.12.037
26. N. Sudhakar, K.P. Rajeev, A.K. Nigam, Low temperature magnetization and magnetoresistance studies on the layered manganite system $La_{1.2}Sr_{1.8}Mn_{2-x}Ru_xO_7$ (x = 0, 0.1, 0.5, 10). Solid State Commun. **132**(9), 635–640 (2004). https://doi.org/10.1016/j.ssc.2004.08.012
27. J.W. Freeland et al., Full bulk spin polarization and intrinsic tunnel barriers at the surface of layered manganites. Nat. Mater. (2005). https://doi.org/10.1038/nmat1280
28. N. Khare, A.K. Gupta, G.L. Bhalla, Preparation and low field magnetoresistance of double layered manganite $La_{1.4}Ca_{1.6}Mn_2O_7$. J. Phys. Chem. Solids **66**(6), 949–953 (2005). https://doi.org/10.1016/j.jpcs.2004.10.014
29. A.K. Gupta, G.L. Bhalla, N. Khare, Magnetic phase diagram of double-layered $La_{2-2x}Ca_{1+2x}Mn_2O_7$ manganite. J. Phys. Chem. Solids **67**(11), 2358–2364 (2006). https://doi.org/10.1016/j.jpcs.2006.06.009
30. A.K. Gupta, R. Kumar, V. Kumar, G.L. Bhalla, N. Khare, Study of magnetotransport in double-layered $La_{1.4}Ca_{1.6}Mn_2O_7$ manganite: presence of nano-ferromagnetic domains in paramagnetic matrix. J. Phys. Chem. Solids **70**(1), 117–121 (2009). https://doi.org/10.1016/j.jpcs.2008.09.010
31. E. Taşarkuyu et al., Effect of high temperature sintering on the structural and the magnetic properties of $La_{1.4}Ca_{1.6}Mn_2O_7$. J. Alloys Compd. **509**(9), 3717–3722 (2011). https://doi.org/10.1016/j.jallcom.2010.12.011
32. A. Belkahla, K. Cherif, J. Dhahri, E.K. Hlil, Magnetic, magnetocaloric properties, and critical behavior in a layered perovskite $La_{1.4}(Sr_{0.95}Ca_{0.05})_{1.6}Mn_2O_7$. J. Mater. Sci. **51**(16), 7636–7651 (2016). https://doi.org/10.1007/s10853-016-0046-x
33. Y.S. Reddy, Electrical transport and magnetoresistance of double layered CMR manganites $R_{1.2}Sr_{1.8}Mn_2O_7$ (R = La, Pr, Sm). Mater. Sci. Pol. **35**(2), 440–446 (2017). https://doi.org/10.1515/msp-2017-0048

34. D. Rybicki, M. Sikora, J. Przewoznik, C. Kapusta, J.F. Mitchell, Interplay of local structure, charge, and spin in bilayered manganese perovskites. Phys. Rev. B **97**(11), 1–8 (2018). https://doi.org/10.1103/PhysRevB.97.115158
35. N.S. Koc, S.P. Altintas, N. Mahamdioua, C. Terzioglu, Cation size mismatch effect in $(La_{1-y}RE_y)_{1.4}Ca_{1.6}Mn_2O_7$ perovskite manganites. J. Alloys Compd. **797**, 471–476 (2019). https://doi.org/10.1016/j.jallcom.2019.05.079
36. Y.S. Reddy, P. Kistaiah, C. Vishnuvardhan Reddy, Elastic properties of double layered manganites $R_{1.2}Sr_{1.8}Mn_2O_7$ (R = La, Pr, Nd, Sm). Rare Met. **33**(2), 166–170 (2014). https://doi.org/10.1007/s12598-013-0128-8
37. R. Terzioglu, The structural and mechanical properties of Gd and Nd substituted double layered $LaCaMnO_7$ ceramics. J. Alloys Compd. **797**, 1173–1180 (2019). https://doi.org/10.1016/j.jallcom.2019.05.191
38. S.P. Altintas, Structural and microhardness studies of rare-earth doped Ruddlesden–Popper manganites. Sak. Univ. J. Sci. **25**(1), 106–118 (2021). https://doi.org/10.16984/saufenbilder.731354
39. R.D. Shannon, Revised effective ionic radii and systematic studies of interatomic distances in halides and chalcogenides. Acta Crystallogr. A **32**(5), 751–767 (1976). https://doi.org/10.1107/S0567739476001551
40. V. Petrícek, M. Dušek, L. Palatinus, Crystallographic computing system JANA2006: general features. Cryst. Mater. **229**(5), 345–352 (2014). https://doi.org/10.1515/zkri-2014-1737
41. P. Scherrer, Bestimmung der inneren Struktur und der Größe von Kolloidteilchen mittels Röntgenstrahlen. Kolloidchem. Ein Lehrb. **40**, 387–409 (1912). https://doi.org/10.1007/978-3-662-33915-2_7
42. A.J.C. Wilson, J.I. Langford, Scherrer after Sixty Years: a Survey and some New results in the determination of Crystallite size. J. Appl. Crystallogr. **11**, 102–113 (1978)
43. A.K. Bhunia, P.K. Jha, S. Saha, Optical and structural characterization of ZnO nanoparticles for binding analysis with semen sample by isothermal titration calorimetry. Bionanoscience **10**(4), 917–927 (2020). https://doi.org/10.1007/s12668-020-00788-0
44. A.K. Bhunia, T. Kamilya, S. Saha, Temperature dependent and kinetic study of the adsorption of bovine serum albumin to ZnO nanoparticle surfaces. ChemistrySelect **1**(11), 2872–2882 (2016). https://doi.org/10.1002/slct.201600446
45. A.K. Bhunia, S. Saha, Characterization of zinc oxide nanocrystals with different morphology for application in ultraviolet-light photocatalytic performances on Rhodamine B. Luminescence **36**(1), 149–162 (2021). https://doi.org/10.1002/bio.3930
46. H. Asano, J. Hayakawa, M. Matsui, Two-dimensional ferromagnetic ordering and magnetoresistance in the layered perovskite. Phys. Rev. B **56**(9), 5395–5403 (1997). https://doi.org/10.1103/PhysRevB.56.5395
47. N. Mahamdioua, A. Amira, S.P. Altintas, A. Varilci, C. Terzioglu, Effect of Re doping on structure and magneto-electrical properties of $La_{1.2}Re_{0.2}Ca_{1.6}Mn_2O_7$ manganites. Physica B **429**, 12–17 (2013). https://doi.org/10.1016/j.physb.2013.07.027
48. A.N. Ulyanov, D.-Q. Hoang, N.N. Kuznetsova, S.-C. Yu, Negative imaginary component of AC magnetic susceptibility, metastable states, and magnetic relaxation in $La_{0.6}Sr_{0.35}MnTi_{0.05}O_3$. Funct. Mater. Lett. **13**(04), 2050023 (2020). https://doi.org/10.1142/S179360472050023X
49. N. Khare, A.K. Gupta, G.L. Bhalla, Low field magnetoresistance and conduction noise in layered manganite $La_{1.4}Ca_{1.6}Mn_2O_7$. Solid State Commun. **132**(11), 799–803 (2004). https://doi.org/10.1016/j.ssc.2004.09.002
50. S.D. Bhame, J.F. Fagnard, M. Pekala, P. Vanderbemden, B. Vertruyen, $La_{0.7}Ca_{0.3}MnO_3/Mn_3O_4$ composites: does an insulating secondary phase always enhance the low field magnetoresistance of manganites. J. Appl. Phys. **111**(6), 063905 (2012). https://doi.org/10.1063/1.3694664
51. D.S. Stone, J.E. Jakes, J. Puthoff, A.A. Elmustafa, Analysis of indentation creep. J. Mater. Res. **25**(4), 611–621 (2010). https://doi.org/10.1557/JMR.2010.0092
52. F. Pöhl, Pop-in behavior and elastic-to-plastic transition of polycrystalline pure iron during sharp nanoindentation. Sci. Rep. **9**(1), 1–12 (2019). https://doi.org/10.1038/s41598-019-51644-5
53. N. Mahamdioua, A. Amira, S.P. Altintas, A. Varilci, C. Terzioglu, Structural and magnetotransport properties of the Y doped A-site deficient double layered manganites $La_{1.2-x-\square_{0.2}}Y_xCa_{1.6}Mn_2O_7$. J. Solid State Chem. **240**, 1–8 (2016). https://doi.org/10.1016/j.jssc.2016.05.011
54. I.G. Berzina, P.A. Savintsev, Effect of irradiation on the contact melting of Metals. In *Surface Phenomena in Metallurgical Processes* (Springer New York, 1965), pp. 186–192
55. R.K. Banerjee, P. Feltham, Deformation and fracture of germanium single crystals. J. Mater. Sci. **9**(9), 1478–1482 (1974). https://doi.org/10.1007/BF00552933
56. K. Sangwal, Microhardness of as-grown and annealed lead sulphide crystals. J. Mater. Sci. **24**(3), 1128–1132 (1989). https://doi.org/10.1007/BF01148809
57. P. Feltham, R. Banerjee, Theory and application of microindentation in studies of glide and cracking in single crystals of elemental and compound semiconductors. J. Mater. Sci. **27**(6), 1626–1632 (1992). https://doi.org/10.1007/BF00542926

58. K. Sangwal, On the reverse indentation size effect and microhardness measurement of solids. Mater. Chem. Phys. **63**(2), 145–152 (2000). https://doi.org/10.1016/S0254-0584(99)00216-3
59. E. Asikuzun, O. Ozturk, L. Arda, D. Akcan, S.D. Senol, C. Terzioglu, Preparation, structural and micromechanical properties of (Al/Mg) co-doped ZnO nanoparticles by sol–gel process. J. Mater. Sci. Mater. Electron. **26**(10), 8147–8159 (2015). https://doi.org/10.1007/s10854-015-3475-4
60. M. Moner-Girona, A. Roig, E. Molins, E. Martínez, J. Esteve, Micromechanical properties of silica aerogels. Appl. Phys. Lett. **75**(5), 653–655 (1999). https://doi.org/10.1063/1.124471
61. J. Makni-Chakroun, W. Cheikhrouhou-Koubaa, M. Koubaa, A. Cheikhrouhou, Impact of a small amount of vacancy in both lanthanum and calcium on the physical properties of nanocrystalline $La_{0.7}Ca_{0.3}MnO_3$ manganite. J. Alloys Compd. **650**, 421–429 (2015). https://doi.org/10.1016/j.jallcom.2015.07.052
62. E. Sellami-Jmal, A. Ezaami, W. Cheikhrouhou-Koubaa, A. Cheikhrouhou, Investigation on physical properties in lanthanum vacancy of $La_{0.65}Ca_{0.35}MnO_3$ elaborated at high temperature. J. Magn. Magn. Mater. **465**, 762–767 (2018). https://doi.org/10.1016/j.jmmm.2018.06.013